Chemical Science

Accepted Manuscript

This article can be cited before page numbers have been issued, to do this please use: Y. Wu, S. Zhou, Z. Luo, S. Yang, Z. Li, Y. Dong, W. Hua, Q. Shuai, D. Dai, M. N. R. Ashfold, K. Yuan and X. Yang, *Chem. Sci.*, 2025, DOI: 10.1039/D5SC04716A.

ROYAL SOCIETY OF CHEMISTRY

rsc.li/chemical-science

Ultraviolet photodissociation of methanethiol (CH_3SH): Revealing an $S(^1D)$ atom elimination channel

Yucheng Wu[1,2], Shunyang Zhou[1], Zijie Luo[1,3], Shuaikang Yang[1], Zhenxing Li[4], Yongxin Dong[3], Wei Hua[1], Quan Shuai[1], Dongxu Dai[1], Michael N.R. Ashfold[5*], Kaijun Yuan[1,2,6*], Xueming Yang.[1,6,7]

1. State Key Laboratory of Chemical Reaction Dynamics and Dalian Coherent Light Source, Dalian Institute of Chemical Physics, Chinese Academy of Sciences, 457 Zhongshan Road, Dalian, 116023, China.
2. University of Chinese Academy of Sciences, Beijing 100049, China.
3. Marine Engineering College, Dalian Maritime University, Liaoning, 116026, China.
4. Institute of Advanced Light Source Facilities, Shenzhen, Guangdong, 518100, China.
5. School of Chemistry, University of Bristol, Bristol, BS8 1TS, U.K.
6. Hefei National Laboratory, Hefei 230088, China.
7. Department of Chemistry and Center for Advanced Light Source Research, College of Science, Southern University of Science and Technology, Shenzhen 518055, China.

* To whom correspondence should be addressed. E-mail addresses: kjyuan@dicp.ac.cn, mike.ashfold@bristol.ac.uk.

View Article Online
DOI: 10.1039/D5SC04716A

Abstract

We report time-sliced velocity map imaging studies of the methyl (CH_3) and electronically excited sulfur ($S(^1D)$) fragments formed following photoexcitation of jet-cooled CH_3SH molecules in the $2^1A'' \leftarrow \tilde{X}\ ^1A'$ absorption band (*i.e.* at wavelengths in the range $190 \leq \lambda \leq 210$ nm). Analyses of images of CH_3 fragments in their $v_2 = 0$, 1 and 2 vibrational levels confirm the perpendicular parent transition dipole moment, prompt bond fission, and show that the ground state SH(X) partners are formed with an inverted vibrational population distribution, peaking at $v = 2$ at the shortest excitation wavelengths investigated. Most of the photolysis photon energy above that required to break the C–S bond is partitioned into product translational energy, however. Primary $S(^1D)$ products are observed when exciting at $\lambda \leq 204$ nm and their relative yield is deduced to increase quite steeply with decreasing wavelength, but quantum yield estimates are beyond the scope of the present work. Image analysis reveals that the CH_4 partners are formed with a highly inverted vibrational population distribution, largely concentrated in the ν_4 bending mode. A possible formation mechanism for the $S(^1D) + CH_4$ products is suggested, based on frustrated C–S bond extension on the initially populated $2^1A''$ potential energy surface (PES) and re-collision between the embryonic CH_3 and SH moieties in the extended region of conical intersection between the $2^1A''$ and $1^1A''$ PESs *en route* to the target products. Cutting edge electronic structure calculations along with complementary *ab initio* molecular dynamics studies should help validate or overturn this envisaged mechanism.

1. Introduction

View Article Online
DOI: 10.1039/D3SC04716A

Metabolization of dimethylsulfoniopropionate (DMSP) produced by phytoplankton and other marine organisms in seawater is recognised as the major biogenic source of dimethyl sulfide (DMS) on Earth. Once emitted into the atmosphere, DMS is rapidly oxidized to become an important precursor of sulfated aerosols and cloud condensation nuclei.[1] Microbial action can also demethylate DMSP to methanethiol (CH_3SH),[2] but the roles of CH_3SH in the oceans and the atmosphere are only now starting to be explored at levels of detail similar to that hitherto focussed on DMS.[3-8] The long wavelength end of the electronic absorption by CH_3SH lies at ultraviolet (UV) wavelengths close to the short wavelength end of the solar spectrum that penetrates through the ozone layer, however, so CH_3SH destruction in the troposphere is by reaction (notably oxidation by OH radicals [9]), not photochemistry.

More widely, sulfur is one of the more abundant elements in the Universe. The S/H ratio in the solar photosphere is $\sim 1.3\times10^{-5}$ (ref. 10), though the deduced quantity of S-containing species in dense clouds in the interstellar medium (ISM) is currently far lower than this quoted cosmic abundance.[11] One plausible explanation for this apparent depletion is that much of the sulfur is incorporated and processed within dust grains and icy mantles. The relative abundance and mobility of hydrogen in an ice matrix suggests that most of the sulfur released by sputtering, thermal- or photo-desorption from such surfaces will be in the form of H_2S,[12] but similar mechanisms could give rise to CH_3SH in the ISM.[13] CH_3SH was first detected tentatively,[14] then definitively,[15] towards the prolific high-mass star-forming region Sagittarius B2 close to the Galactic center, and has subsequently been observed in a range of locations, *e.g.* towards the organic hot-core G327.3-06,[16] the cold core B1,[17] the dense, warm part of a high-mass star-forming region in Orion,[18] in the vicinity of the solar type protostar IRAS 16293-2422 [19] and the prestellar core L1544,[20] in both the cold envelope and the hot gas around Cyg X-N12 [21] and in the hot gas surrounding G328.2551-0.5321.[22] The tentative identification of DMS in the atmosphere surrounding exoplanet K2-18 [23] has fuelled debate regarding the possibility of life on planets other than Earth, but other recent observational [24] and laboratory [25] studies serve as a reminder that DMS may also arise via abiotic routes.

Photodissociation can be an important contributor to CH_3SH destruction in many regions of the ISM. As noted above, the electronic absorption of CH_3SH is concentrated in the UV spectral region,[26-29] comprising a broad region of continuous absorption that peaks at $\lambda \sim 235$ nm and extends to beyond 300 nm and more localised, structured Rydberg features at shorter wavelengths converging towards the first ionisation potential (IP = 9.2922±0.0007 eV, corresponding to an excitation wavelength $\lambda = 133.4$ nm).[30] Photoexcitation within the first

View Article Online
DOI: 10.1039/D5SC04716A

absorption band promotes an electron from the highest occupied molecular orbital (HOMO, a non-bonding 3p orbital centred on the S atom) to an excited orbital with mixed Rydberg (4s) / valence (σ*) character. [31,32] The resulting $1^1A''$ excited state is dissociative with respect to both the H_3CS–H and H_3C–SH bond extension coordinates (henceforth $R_{S–H}$ and $R_{C–S}$, respectively), though the $1^1A''$ potential energy surface (PES) displays a modest barrier at short C–S separations. Prompt S–H bond rupture is thus the dominant fate when exciting CH_3SH at long wavelengths. The resulting $CH_3S(\tilde{X})$ fragments are formed with modest vibrational excitation in the ν_3 (C–S stretch) mode, but most of the photon energy in excess of that required to break the S–H bond ($D_0(H_3CS–H)$ = 30250±100 cm^{-1}, ref. 33) is partitioned into product translational motion along axes that are preferentially perpendicular to the transition dipole moment (and thus to the polarization vector **ε** of the photolysis laser radiation).[33,34] The $CH_3(v=0)$ fragment images recorded when exciting CH_3SH in the range 220 ≤ λ ≤ 233 nm also display near limiting perpendicular recoil anisotropy and show that most of the partner SH(X) fragments are formed in their ground vibrational state.[35] The relative yield of CH_3 + SH products increases on tuning to shorter wavelengths,[36] particularly when exciting the more localised $2^1A''\leftarrow\tilde{X}^1A'$ band that dominates the absorption spectrum at wavelengths in the range 190 ≤ λ ≤ 215 nm, such that the two channels have similar quantum yields when photolyzing at λ = 193 nm.[37]

The present work involves detailed study of photofragmentation pathways following excitation of CH_3SH within the $2^1A''\leftarrow\tilde{X}^1A'$ absorption band. The parent absorption spectrum at wavelengths around this transition is shown in Figure 1, along with arrows showing the species probed at each wavelength investigated. This transition is attributed to a 4p/4s(a′)←HOMO(a″) electron promotion. The adiabatic $2^1A''$ state is bound with respect to extending $R_{S–H}$ or $R_{C–S}$, but both dissociation coordinates can be accessed via efficient non-adiabatic coupling at a region of conical intersection (CI) between the $2^1A''$ and $1^1A''$ PESs in the near vertical Franck-Condon region.[31,32,38,39] Prior studies at λ = 208 nm [33] and 193 nm [34] revealed substantial vibrational excitation in the $CH_3S(\tilde{X})$ fragments from the former channel, most notably an obvious progression in the ν_3(C–S) stretch mode. This points to some significant coupling between the C–S and S–H stretch motions during the dissociation process and the likely inadequacy of any one-dimensional representation of what is an inherently multi-dimensional problem.[38,39] CH_3 fragments from the latter channel have been detected, generally with vibrational state specificity, following excitation at several wavelengths in the range 202 ≤ λ ≤ 210 nm.[35,40-42] The SH(X) partners formed at these shorter excitation wavelengths

View Article Online
DOI: 10.1039/D3SC04716A

populate a range of vibrational (v) states, with distributions that peak at $v > 0$. The products from both channels again display preferential perpendicular recoil anisotropy, implying that non-adiabatic coupling via the $2^1A''/1^1A''$ CI is efficient and that dissociation occurs on a timescale comparable to, or faster than, the rotational period of the jet-cooled parent CH_3SH molecules.

Dissociation channels (1) and (2) are just two of many thermochemically allowed decay channels available to CH_3SH molecules when excited at λ ~200 nm, however. Focussing on spin-allowed fragmentation processes yielding two products,

$$CH_3SH + h\nu \rightarrow CH_3 + SH \qquad E_{th} = 25340 \pm 40 \text{ cm}^{-1} \qquad (1)$$

$$\rightarrow CH_3S + H \qquad E_{th} = 30250 \pm 100 \text{ cm}^{-1}, \qquad (2)$$

could be supplemented by one or more of the following fragmentations

$$CH_3SH + h\nu \rightarrow H_2CS + H_2 \qquad E_{th} = 11000 \pm 200 \text{ cm}^{-1} \qquad (3)$$

$$\rightarrow S(^1D) + CH_4 \qquad E_{th} = 27690 \pm 40 \text{ cm}^{-1} \qquad (4)$$

$$\rightarrow CH_2(\tilde{a}^1A_1) + H_2S \qquad E_{th} = 35260 \pm 40 \text{ cm}^{-1}, \qquad (5)$$

and dissociations yielding products in higher excited states, *e.g.*

$$CH_3SH + h\nu \rightarrow H_2CS(\tilde{A}) + H_2 \qquad E_{th} = 27400 \pm 200 \text{ cm}^{-1} \qquad (6)$$

$$\rightarrow S(^1S) + CH_4 \qquad E_{th} = 40630 \pm 40 \text{ cm}^{-1}, \qquad (7)$$

though we recognise that the energetic onsets for many of these later eliminations may be higher than these quoted thermochemical threshold (E_{th}) values as the process is likely to involve passage over an energy barrier. Inclusion of spin forbidden dissociations yielding, *e.g.*, $S(^3P)$ atoms or triplet state CH_2 radicals or excited triplet state H_2CS molecules (processes not currently included in this list) opens the range of possible dissociation processes yet further, and the onset of the lowest energy three-body dissociation channel (8) is only just above the energy of a λ = 200 nm photon.

$$CH_3SH + h\nu \rightarrow CH_3 + S(^3P) + H \qquad E_{th} = 53730 \pm 40 \text{ cm}^{-1}. \qquad (8)$$

The $D_0(H_3CS–H)$ value quoted for dissociation (2) is from ref. 33. All other threshold energies quoted here are derived using $\Delta_f H^o(0\text{ K})$ values and uncertainties from ref. 43 and atomic term

View Article Online
DOI: 10.1039/D5SC04716A

values from ref. 44, while the Ã–X̃ term value for thioformaldehyde used in determining E_T(6) is from Jacox.[45]

H_2CS formation was predicted in early photolysis studies of CH_3SH at λ = 185 nm [46] and identified in later time-of-flight mass spectrometry measurements following CH_3SH photolysis at the ArF laser wavelength (193.3 nm).[47] S(^{3}P) and S(^{1}D) atoms have been detected following 193.3 nm excitation of CH_3SH but, from measurements of the signal dependence upon photolysis laser intensity, these were deduced to arise from secondary photolysis of primary CH_3S and/or SH photoproducts.[48] The present work extends high resolution imaging measurements of the $CH_3(v)$ products down to the short wavelength end of the $2^1A''\leftarrow\tilde{X}^1A'$ absorption band, *i.e.* λ ≥191 nm (Fig. 1), thereby enabling new insights into dissociation process (1), and provides first and definitive evidence for the operation of the rival dissociation channel (4) yielding S(^{1}D) + CH_4 products.

2. Experimental

The experiments employed a time-sliced velocity map ion imaging (TS-VMI) detection apparatus, details of which have been reported previously,[49-54] along with UV photolysis laser pulses in the range 190 ≤ λ ≤ 240 nm and both UV and vacuum UV (VUV) probe laser pulses to detect, respectively $CH_3(v)$ and S(^{1}D) photofragments. The CH_3SH sample was introduced into the source chamber as a pulsed supersonic beam (10% CH_3SH in Ar, Kylingas (99.5% purity)), where it was skimmed prior to entering (through a 2 mm hole in the first electrode) and propagating along the centre axis of the 23-plate ion optics assembly (IOA) within the spectrometer. The photolysis and probe laser beams intercepted the pulsed molecular beam at right angles, between the second and third plates of the IOA.

The requisite UV photolysis wavelengths were generated by frequency doubling or sum--frequency mixing using a table-top laser system. Light at λ ≥ 204 nm (~1 mJ pulse^{-1}, pulse duration ~10 ns) was produced by frequency doubling the output of a dye laser (Sirah, PESC-G-24) pumped by the third harmonic (355 nm) output of a Nd:YAG laser (Continuum PL-9030). As such, the photolysis photon wavenumber in all cases was defined to sub-cm^{-1} precision; the wavelengths used were chosen to be a whole number of nm. Light in the wavelength range 191 ≤ λ ≤ 199 nm (~0.3 mJ pulse^{-1}, pulse duration ~10 ns) was generated as the sum (*i.e.* $\omega_1 + \omega_2$) frequency output using a BBO crystal, with ω_1 set at the frequency corresponding to λ_1 = 266 nm (produced by frequency doubling the output of a 355 nm (the

View Article Online
DOI: 10.1039/D3SC04716A

third harmonic output of a Continuum PL-9030 Nd:YAG laser) pumped dye laser (Sirah, PESC-G-24) operating at λ ~532 nm). The requisite ω_2 frequencies were produced using half of the second harmonic (532 nm) output from the same Continuum Nd:YAG laser to pump another dye laser (Sirah, PESC-G-24) generating photons with λ_2 wavelengths in the range 677-790 nm (~8-10 mJ pulse^{-1}, duration of ~10 ns).

S(^{1}D) photoproducts were probed by Doppler scanning back and forth across the one photon absorption at λ = 130.091 nm, which populates the autoionizing $3p^3(^2D^o)5s$; $^1D_2{}^o$ level of atomic sulfur. As previously,[50,55,56] these VUV photons were generated by four wave difference (*i.e.* $2\omega_3 - \omega_4$) frequency mixing of the frequency doubled output from one dye laser (at λ_3 = 212.556 nm) with the fundamental output of a second dye laser (at λ_4 = 580.654 nm) in a Kr/Ar gas mixture. The contrast between the structured and underlying continuum two-colour contributions to the S(^{1}D) images was boosted by deliberately shifting the focus of the photolysis laser radiation 8 cm away from the interaction region, by translating the position of the 50 cm focal length lens used to focus this radiation. $CH_3(\tilde{X}, v)$ photoproducts were probed by two photon resonance enhanced multiphoton ionization (2+1 REMPI) using documented excitation wavelengths in the range 325 ≤ λ ≤ 333.5 nm to sample population in the v=0, v_2=1, v_2=2 and v_1=1 levels,[57,58] as described elsewhere.[59] The requisite UV pulses (~2 mJ pulse^{-1}, duration of ~10 ns) were produced by frequency doubling the output of another (Sirah, PESC-G-24) dye laser operating at λ ~650-667 nm, which was pumped by the other half of the 532 nm output from the above Nd-YAG laser. The polarization vectors of the photolysis ($\boldsymbol{\varepsilon_{phot}}$) and probe ($\boldsymbol{\varepsilon_{probe}}$) laser radiation were both parallel to the front face of the detector, and the crossing angle between the photolysis and REMPI probe laser beam paths in the interaction region was ~7°, where the time delay between the respective pulses was in the range 10-20 ns.

The resulting S^+/CH_3^+ ions were accelerated through the rest of the IOA and detected with a dual microchannel plate assembly coupled with a P43 phosphor screen at the end of the 740 mm ion flight tube. The detector was time gated (15-20 ns) to select ions with m/z 32 (S^+) or 15 (CH_3^+) and to confirm that the signal was from the intended two-colour UV photolysis – REMPI/VUV probe scheme, three images were recorded for each set of experimental conditions with: (i) both the photolysis and probe beams present in the interaction region; (ii) the photolysis beam present but the probe beam blocked, and (iii) the photolysis beam blocked and the probe beam present. For all two-colour images displayed in this article, the one-colour

photoinduced background images recorded under conditions (ii) and (iii) have already been subtracted from the image recorded under condition (i).

3. Results

3.1 CH_3 fragment imaging

Figure 2 shows TS-VM images of the $CH_3(v=0)$ fragments obtained following photolysis of the jet-cooled CH_3SH sample at λ = 199, 196 and 193 nm, at the high energy end of the $2^1A''\leftarrow\tilde{X}^1A'$ absorption band. Corresponding images of CH_3 products formed in the $v_2=1$ and $v_2=2$ levels (where ν_2 is the out-of-plane umbrella bending mode) are shown in Figs. S1 and S2 in the Electronic Supplementary Information (ESI). In all cases, $\boldsymbol{\varepsilon_{phot}}$ is in the plane of the image, as shown by the double headed arrow included in panel (a) of each of these figures. Analysis of such images allows determination of (i) the total kinetic energy release, $P(E_T)$, distributions, given the provisos of two body dissociation, momentum conservation and the partner fragment being SH, and (ii) the (E_T-dependent) recoil anisotropy. The latter is defined in terms of the anisotropy parameter, β, which is obtained by fitting the measured intensities to the expression $I(\theta) \propto [1 + \beta(P_2(\cos\theta)]$, where θ defines the angle of the recoil velocity vector relative to $\boldsymbol{\varepsilon_{phot}}$ and $P_2(\cos\theta)$ is the second Legendre polynomial. β takes limiting values of +2 and –1 in the case of axial recoil following one photon excitation via a transition dipole moment that lies, respectively, parallel and perpendicular to the breaking bond. The $P(E_T)$ and $\beta(E_T)$ plots (black and blue, respectively) are shown to the right of the corresponding images in Figs. 2, S1 and S2.

Each image shows a structured, anisotropic ring at large radius and a secondary feature concentrated at the image centre. The former arises from the target process (1). The latter feature has been observed previously following excitation at other wavelengths in this region,[35,41,42] and is logically attributed to CH_3 fragments arising via unwanted probe-laser-induced photolysis of $CH_3S(\tilde{X})$ fragments formed via the rival primary fragmentation channel (2).

We consider this latter signal first. The thermochemical threshold energy for process (9)

$$CH_3S + h\nu \rightarrow CH_3 + S(^3P) \qquad E_{th} = 24340 \pm 100\ cm^{-1} \qquad (9)$$

can be derived from the documented $D_0(H_3CS–H)$ value [33] and the relevant $\Delta_f H^o(0\ K)$ values given in ref. 43. The wavelength of the probe photons used for $CH_3(v=0)$ detection (λ = 333.46

nm, corresponding to a wavenumber of 29988.6 cm^{-1}) falls within the $CH_3S(\tilde{A}–\tilde{X})$ absorption band.[60-62] The resulting $CH_3S(A)$ fragments predissociate to $CH_3 + S(^3P)$ products (process (9)), most of which display preferential perpendicular recoil anisotropy.[63,64] $CH_3(v=0)$ fragments arising via one probe laser photon induced photolysis of primary $CH_3S(\tilde{X}, v=0)$ fragments should thus appear with E_T ~5600 cm^{-1}. Several factors serve to blur such an analysis for the present experiments, however. The primary $CH_3S(\tilde{X})$ fragments from λ ~200 nm photolysis of CH_3SH are formed with a range of kinetic energies, though momentum conservation ensures that most of any E_T released in dissociation process (2) is carried by the light H atom partner. More importantly, the $CH_3S(\tilde{X})$ fragments are distributed over a range of vibrational states, some with internal energies (E_{int}) approaching the limit allowed by energy conservation.[33,34] The relative absorption cross-sections of $CH_3S(\tilde{X})$ fragments in different v levels at the probe wavelength of interest is not known, nor are many details of the dissociation dynamics of different $CH_3S(\tilde{A}, v)$ fragments. Conceivably, however, the probe-laser induced photodissociation of primary $CH_3S(\tilde{X})$ fragments in high E_{int} states could yield $CH_3 + S(^3P)$ products with E_T ~15000 cm^{-1} or more, which would overlap with features attributable to CH_3 + SH(X, higher v) products (primary process (1)) in the $P(E_T)$ spectra shown in Figs. 2, S1 and S2. The CH_3 fragments attributed to probe-laser induced photolysis of the ensemble of primary $CH_3S(\tilde{X})$ products show some preferential perpendicular recoil anisotropy (Fig. S1).

We now focus on the feature at larger radius in these $CH_3(v)$ images. As shown by the combs superposed above the $P(E_T)$ distributions derived from the $CH_3(v=0)$, $CH_3(v_2=1)$ and $CH_3(v_2=2)$ images shown in Figs. 2, S1 and S2, the partner SH(X) fragments are formed in levels with v up to ~6. For any set of $CH_3(v; \lambda)$ images, the onset at high E_T associated with formation of $SH(v=0)$ co-fragments shows the expected shift to higher E_T as the photolysis wavelength is reduced. More strikingly, the most populated level in the SH(v) population distribution, $P(v)$, clearly increases from $v = 1$ to $v = 2$ as the photolysis wavelength is decreased from 199 nm to 193 nm, but the various $P(v)$ distributions appear to be relatively insensitive to the probed $CH_3(v)$ level. No signal attributable to $CH_3(v_1=1)$ fragments was observed when exciting at the probe wavelength recommended [58] for their detection. The SH product vibrational energy distributions can be put on a more quantitative footing by fitting the higher-E_T part of the $P(E_T)$ distributions using a set of suitably positioned Gaussian functions to represent the different SH(v) levels. An illustrative decomposition of the data obtained at λ = 196 nm is shown in Fig. S3. Note, the signal attributable to secondary photolysis of primary

View Article Online
DOI: 10.1039/D5SC04716A

CH_3S fragments is likely to extend to E_T values attributed to primary CH_3 + SH(X, v = 5 and, particularly, 6) products, so the present analysis almost certainly overestimates the relative yields of these SH(X, high v) levels. The overlapping contributions from these two CH_3 radical sources may be responsible for the apparent reduction in the recoil anisotropy of the CH_3 + SH(X, higher v) products.

Fig. 3(b) shows the SH $P(v)$ distributions deduced from analysing the $CH_3(v=0)$ images obtained at λ = 199, 196 and 193 nm. These data are supplemented by the corresponding $P(v)$ distributions reported previously following photolysis at λ = 204 nm [41] and 210 nm.[42] SH $P(v)$ distributions determined when exciting at longer wavelengths (in the $1^1A''\leftarrow\tilde{X}^1A'$ absorption continuum) are shown in Fig. 3(a). The λ = 235 and 240 nm data are derived from $P(E_T)$ spectra recorded as part of the present study (shown in Fig. S4 in the ESI), while the SH $P(v)$ distributions from CH_3SH photolysis at λ = 220, 228 and 233 nm are from ref. 35. These long wavelength data are peripheral to the primary focus of the present paper but are included for completeness. All serve to reinforce previous conclusions that (i) the SH(X) fragments formed by photolysis within the $1^1A''\leftarrow\tilde{X}^1A'$ continuum carry modest vibrational (and modest rotational) excitation, whereas those formed by photolysis in the $2^1A''\leftarrow\tilde{X}^1A'$ band show inverted $P(v)$ distributions, (ii) the energy disposal in the SH(X) fragments formed at any given wavelength is relatively insensitive to any vibrational excitation in the probed $CH_3(\nu_2)$ fragment, and (iii) most of the photon energy in excess of that required to break the C–S bond is partitioned into product translational motion.

3.2 S(^{1}D) fragment imaging

Figures 4(a) and 4(b) show TS-VM images of the S(^{1}D) fragments formed when photolyzing jet-cooled CH_3SH molecules at λ = 192 and 191 nm. As noted in the Experimental section, the focus of the photolysis laser radiation was translated 8 cm from the interaction region to maximise the contrast between the structured signal of most interest from underlying photolysis-laser-induced background signal. Even a cursory examination of these images shows that the S(^{1}D) images recoil along axes perpendicular to $\boldsymbol{\varepsilon_{phot}}$. The left-hand panels in Fig. 5 show the corresponding S(^{1}D) fragment images measured under the same experimental conditions when exciting at λ = (a) 204, (b) 199, (c) 196 and (d) 193 nm. No fine structure was evident in the corresponding image measured at λ = 212 nm, as shown in Fig. S5. The panel to the right of each image shows the corresponding $P(E_T)$ distributions derived from (i) the two-colour image measured with both photolysis and probe lasers present (red trace), (ii) the one-

View Article Online
DOI: 10.1039/D3C04716A

colour probe laser only image (black trace), which peaks at low E_T, and (iii) the difference (*i.e.* red minus black) distribution attributable to real two-colour signal (blue trace). The $\beta(E_T)$ distribution derived from this real two-colour signal is also shown in each right-hand panel (blue points, joined by a dashed line) and the $\beta(E_T)$ distribution for the one colour probe only signal is also included in Figs. 4, 5 and S5 (black dots).

The two-colour images measured at $\lambda \leq 204$ nm contain (at least) three components. The structure attributable to the $S(^1D) + CH_4$ products formed via channel (4) is the feature of greatest novelty but we choose to interpret the overlapping unstructured contributions first. The probe-only signal (black traces in Figs. 4, 5 and S5) is attributable to the probe ($\lambda = 130.091$ nm) laser induced three body dissociation

$$CH_3SH + h\nu \rightarrow CH_3 + S(^1D) + H \qquad E_{th} = 62970 \pm 40 \text{ cm}^{-1}, \qquad (10)$$

products from which, by energy conservation arguments, could appear with $E_T \leq 13900$ cm^{-1}. We note that the E_T values in the $P(E_T)$ traces displayed in Figs. 4, 5 and S5 are derived assuming two body dissociation and that the partner to the imaged S atom has $m = 16$, so are not strictly accurate for products arising via process (10). But the black trace in each plot sensibly declines to the baseline by this predicted upper limit E_T value and peaks at much lower translational energies, implying significant internal excitation in the CH_3 products formed at this VUV wavelength.

The second unstructured contribution lies under the structured features in the real two-colour signal (the blue traces in the displayed $P(E_T)$ spectra) and extends to E_T values much higher than that accessible via one photolysis photon induced formation of $S(^1D) + CH_4$ products. This contribution dominates the spectra recorded at longer wavelengths and is likely responsible for all the two-colour signal in the image measured at $\lambda = 212$ nm (Fig. S5). As Fig. S5 shows, the high E_T limit of this signal is sensibly consistent with that expected from resonance enhanced two-photolysis-photon induced dissociation of CH_3SH via channel (10), *i.e.* $E_T \leq 31370$ cm^{-1} at $\lambda = 212$ nm. Inspection of the corresponding two-colour $P(E_T)$ spectra (blue traces) obtained at shorter wavelengths shows this high energy tail stretching out to progressively high E_T values consistent with the thermochemical prediction that two-photolysis-photon induced dissociation could yield products with $E_T \leq 35070$ cm^{-1} at $\lambda = 204$ nm and $E_T \leq 37530$ cm^{-1} at $\lambda = 199$ nm (Fig. 5). But inspection of Fig. 4 also suggests that this two-photon contribution is comparatively minor in the $S(^1D)$ product images measured at $\lambda =$

191 or 192 nm, *i.e.* that process (4) – which we will now show to be responsible for the structure in these $P(E_T)$ spectra – contributes only weakly at λ = 204 nm but its relative importance increases steeply on tuning to shorter excitation wavelengths within the $2^1A''\leftarrow\tilde{X}^1A'$ absorption band.

From hereon we focus on the structured signal attributed to $S(^1D) + CH_4$ product formation. CH_4 has four normal modes of vibration, that can be labelled by irreducible representations of the T_d point group, according to the symmetry of the associated normal coordinates. These are the symmetric (ν_1) and asymmetric (ν_3) stretching modes, with respective degeneracies of 1 and 3, and the ν_2 and ν_4 bending modes, with respective degeneracies of 2 and 3. The wavenumbers of the two stretch fundamentals are similar. The wavenumbers of ν_2 and ν_4 fundamentals are also similar, and both are about half that of ν_1 and ν_3. This leads to a well-defined polyad structure, with each polyad P_n defined by the integer n, where

$$n = 2(v_1 + v_3) + v_2 + v_4. \qquad (11)$$

The v_i in eq. (11) are the vibrational quantum numbers, and each (v_1, v_2, v_3, v_4) set defines a vibrational level, most of which – because of the degeneracies of the ν_2, ν_3 and ν_4 modes – split into multiple sub-levels. The levels within each polyad span a range of energies, the spread of which increases quite rapidly with n.[65,66] For future reference, we also note that the lowest energy levels within any P_n polyad are those associated with the nv_4 levels.[65,66]

The observed peaks align fairly well with the $E_{T(max)}$ values predicted given the respective UV photon energies, $E_{th}(4)$ and the predicted wavenumber of the centre of gravity of each polyad with $n \leq 9$,[65] but the alignment between the ticks and the peaks degrades with increasing n. Better alignment is achieved by assuming a smaller peak spacing of ~1330 cm^{-1}, shown by the combs superposed above the data in Figs. 4(c) and 4(d) and in the right hand panels in Fig. 5. This hints that the observed peaks are dominated by a sub-set of levels involving multiples of the ν_4 bending mode. Such an interpretation also fits better with the apparent near-constancy of the peak widths, the narrowness of which also implies that the CH_4 fragments must be formed with only modest rotational excitation. As Fig. 6 shows, the vibrational state population distribution, $P(v_4)$, in the CH_4 fragments formed when photolyzing at λ = 192 nm (Fig. 4(a)) is highly inverted, peaking at v_4 = 8 and implying an average vibrational energy content in the CH_4 fragments of ~10000 cm^{-1}. The increased relative contribution to the $S(^1D)$ product yield

View Article Online
DOI: 10.1039/D3SC04716A

from two-photolysis-photon induced dissociations in images recorded at longer wavelengths makes it hard to define any λ-dependence of the $P(v_4)$ distribution. The possible UV photofragmentation dynamics responsible for the deduced S(^{1}D) + CH_4 product state distribution is discussed along with the previously recognised dissociation processes (1) and (2) in the following section.

4. Discussion

The observation and characterization of the hitherto unreported S(^{1}D) + CH_4 product channel (4) following photoexcitation of CH_3SH in the wavelength range $191 \leq \lambda \leq 204$ nm is the most striking finding from the present work. In what follows, we consider possible mechanisms for this process – effectively an elimination of the central atom in an ABC framework to yield B + AC products. Reports of such photo-induced eliminations are becoming increasing commonplace,[52] having recently been recognised in, for example: H_2O (yielding H_2 + O(^{1}S) products),[67] H_2S (yielding H_2 molecules together with a sulfur atom, in the ^{1}D or ^{1}S excited state),[56,68] CO_2,[69] OCS,[70] CS_2,[51] (yielding C(^{3}P) atoms in each case), SO_2 (yielding S(^{1}D) products) [71] and, in a molecule of more similar size to that of present interest, CH_3NH_2 (yielding NH($X^3\Sigma^-$) + CH_4 products).[72,73] These prior studies suggest various (molecule specific) mechanisms for such photo-induced eliminations, amongst which are a class of frustrated dissociations sometimes described as 'roaming'.[74] In such cases, the topography of the excited state potential accessed by photoexcitation drives an initial bond extension, but the available energy is insufficient to enable complete bond fission. The partner moieties are thus drawn back towards one another and undergo what is effectively an intramolecular collision prior to re-separating as (potentially) an alternative product pair. The available data suggests that such a mechanism might account for the S(^{1}D) + CH_4 fragment channel identified in the present work.

First, we reiterate that the operation of rival primary C–S and S–H bond fission processes following photoexcitation to the $2^1A''$ state at λ ~200 nm is well-established. The adiabatic potential of the $2^1A''$ state is bound in both R_{C-S} and R_{S-H}; dissociation occurs on the $1^1A''$ PES, after non-adiabatic coupling in an extended region of CI between the $2^1A''$ and $1^1A''$ potentials.[38,39] The present work reveals some vibrational excitation in the SH(X) fragments formed via channel (1) when exciting in the $190 \leq \lambda \leq 200$ nm range, but also suggests that – as at longer excitation wavelengths – most of the photon energy in excess of that required to break the C–S bond is partitioned into $CH_3(\tilde{X})$ + SH(X) product translational motion.[35,40-42]

The $CH_3S(\tilde{X})$ products arising via the rival channel (2) following excitation to the $2^1A''$ state and subsequent non-adiabatic coupling to the $1^1A''$ PES are distributed over many vibrational levels, with very obvious activity in the ν_3(C–S) stretch mode, but, again, even the most internally excited H + $CH_3S(\tilde{X})$ products recoil with E_T ~1 eV.[33,34] Neither of these pathways obviously satisfy the picture of a frustrated dissociation and re-collision.

Several other points merit note, however. The relative importance of the C–S bond fission process (1) increases markedly once exciting in the $2^1A''\leftarrow\tilde{X}^1A'$ absorption band, suggesting that a larger fraction of the molecules photoexcited at these shorter wavelengths undergo initial C–S bond extension. This accords with the observed ν_5(C–S) stretch progression in the weak emission spectrum from the parent CH_3SH molecules following excitation at λ = 193.3 nm.[36] Additionally, the $2^1A''$ PES is adiabatically bound, correlating to $CH_3(\tilde{X})$ + SH(A) fragments when extending $R_{C–S}$ (and to H + $CH_3S(\tilde{A})$ fragments when extending $R_{S–H}$). Thus it is tempting to speculate that the observed S(^{1}D) + CH_4 products might arise from a fraction of the photoexcited molecules that initially distort by extending $R_{C–S}$, avoid non-adiabatic coupling to the $1^1A''$ PES during this bond extension phase, reach the maximum $R_{C–S}$ value consistent with energy conservation on the $2^1A''$ PES, then re-compress to enable a re-encounter between the CH_3 and SH moieties and, potentially, exothermic reaction on to S(^{1}D) + CH_4 products (4).

Further mechanistic speculation at this stage is unwarranted, but it is very much hoped that the present data will inspire new high-level quantum chemical calculations of the $2^1A''$ and $1^1A''$ PESs and the non-adiabatic coupling between them (and, conceivably, to the $\tilde{X}^1A'$ PES), together with *ab initio* molecular dynamics calculations designed to explore further the dynamics displayed by the products of dissociation processes (1), (2), (4) and, potentially, (3) and (5) – all of which could plausibly arise when exciting CH_3SH at λ ~200 nm. Future studies (experimental and/or theoretical) might also usefully search for processes yielding S(^{3}P) atom products, estimate product quantum yields (branching fractions), and explore how these vary with excitation wavelength. Extension of such contemporary photofragmentation studies to the oxygen analogue, methanol, the simplest and most abundant interstellar complex organic molecule observed in warm and cold environments,[75,76] should be an obvious priority, but searching for singlet products (*e.g.* NH($a^1\Delta$) + CH_4) from photolysis of methylamine could also be very rewarding.

View Article Online
DOI: 10.1039/D5SC04716A

Author contributions

K.J.Y. and X.M.Y. supervised the research. K.J.Y. conceived the research. M.N.R.A. and K.J.Y. designed the experiments. Y.C.W., S.Y.Z., Z.J.L., S.K.Y., Z.X.L., Y.X.D., W.H. and Q.S. performed the experiments. Y.C.W., D.X.D., M.N.R.A., K.J.Y and X.M.Y. analysed the data. Y.C.W., K.J.Y. and M.N.R.A. wrote the manuscript. All authors discussed the results and commented on the manuscript.

Conflicts of interest

There are no conflicts to declare.

Data availability

The data supporting this study are available within the main text and the ESI.

Acknowledgements

The experimental work was supported by the National Natural Science Foundation of China (Grant Nos. 22241304, 22225303, 22403091, 22173100), the Major Program of National Natural Science Foundation of China (Nos. 42494850 and 42494853), the National Natural Science Foundation of China (NSFC Center for Chemical Dynamics (Grant No. 22288201)), the Strategic Priority Research Program of the Chinese Academy of Sciences (Grant Nos. XDB0970000 and XDB0970200), the Innovation Program for Quantum Science and Technology (Grant No. 2021ZD0303304) and the Liaoning Revitalization Talents Program (Grant No. XLYC2402046). X. Yang also thanks the Shenzhen Science and Technology Program (Grant No. ZDSYS20200421111001787), Z. Li thanks the Guangdong Science and Technology Program (Grant No. 2025A1515012671).

Figures and Captions

View Article Online
DOI: 10.1039/D5SC04716A

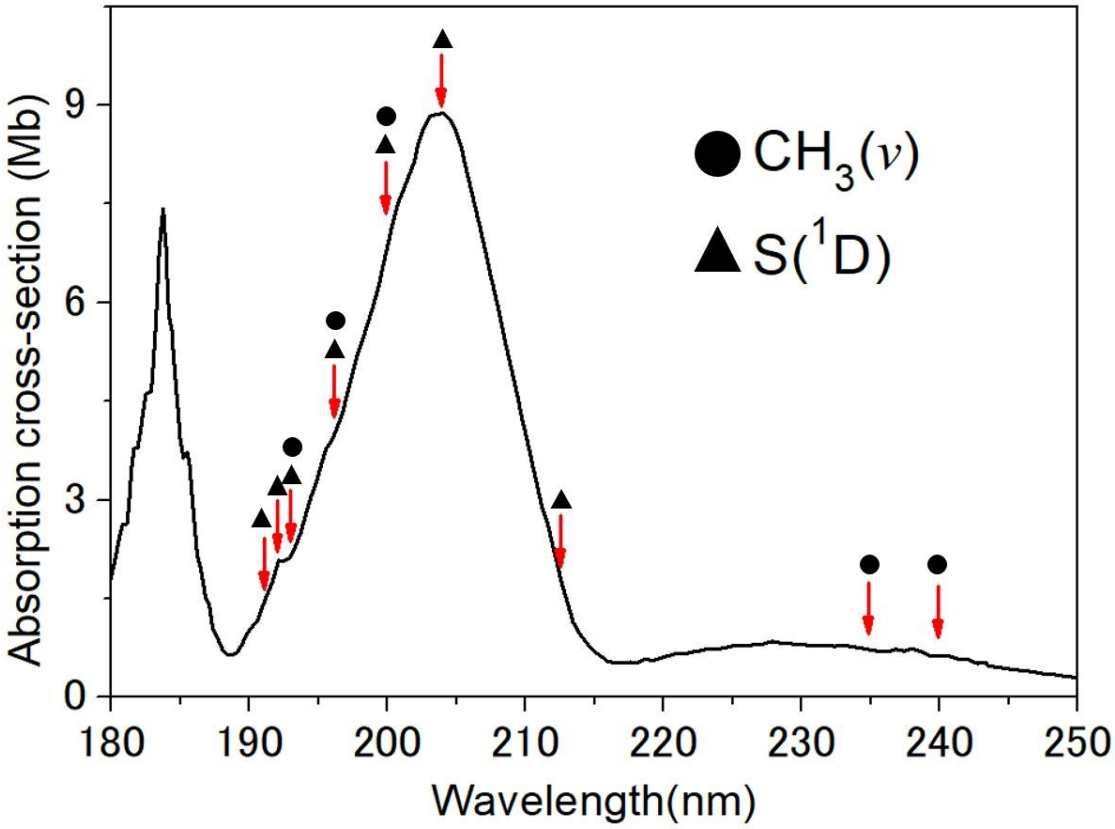

Figure 1. Room temperature absorption spectrum of CH_3SH (after refs. 27 and 29), with the photolysis wavelengths investigated in the present work marked and labelled to show the species probed at each wavelength.

View Article Online
DOI: 10.1039/D5SC04716A

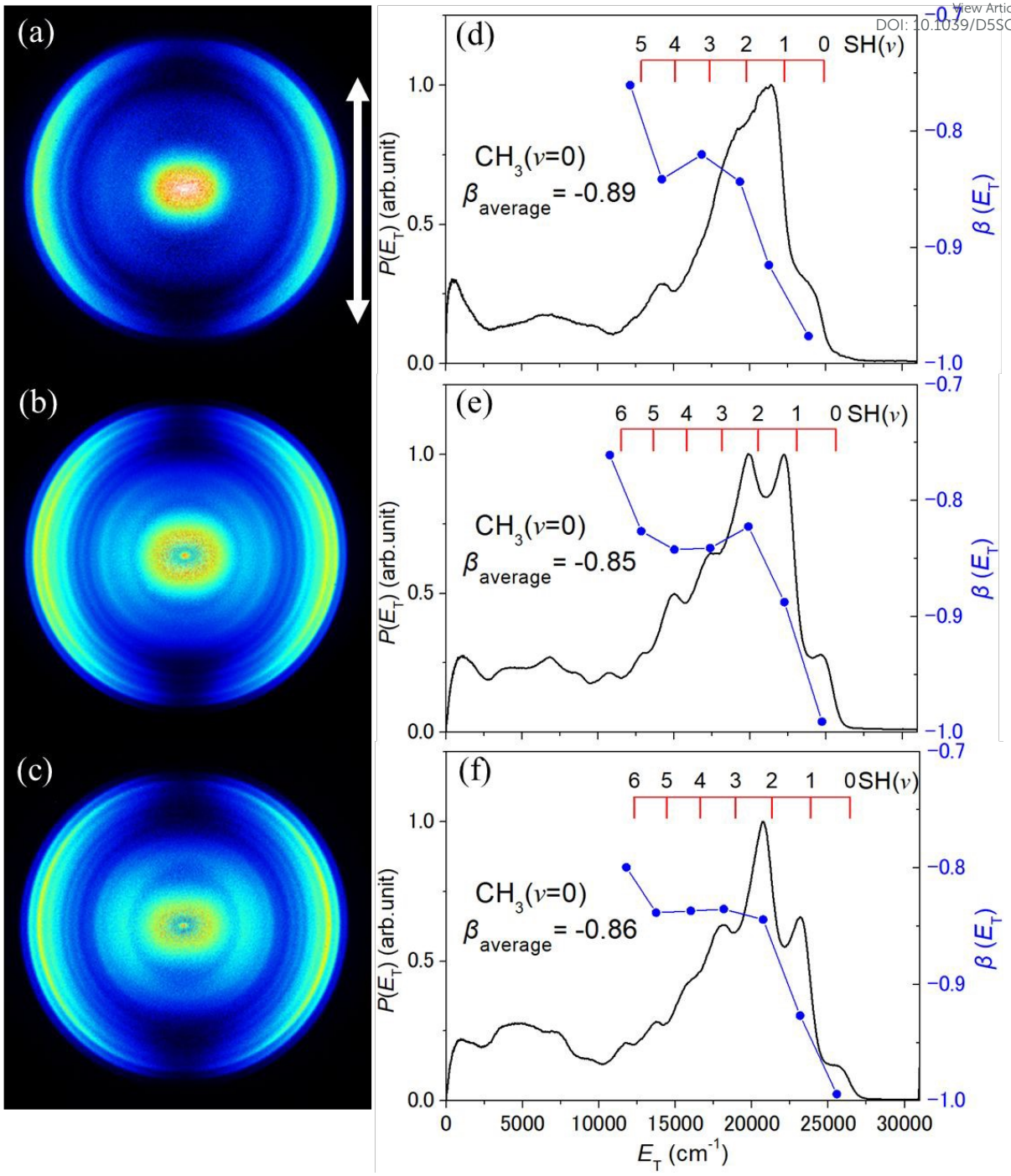

Figure 2. TS-VM images of $CH_3(v=0)$ fragments formed by photolysis of jet-cooled CH_3SH molecules at λ = (a) 199, (b) 196 and (c) 193 nm, with $\boldsymbol{\varepsilon}_{\mathbf{phot}}$ aligned vertically in the plane of the image as indicated by the double headed arrow in (a). The corresponding $P(E_T)$ (black) and $\beta(E_T)$ (blue) distributions derived from each image are displayed in panels (d), (e) and (f), with the relevant scales shown on, respectively, the left- and right-hand *y*-axes, along with the $\beta_{average}$ value determined over the indicated E_T range. The red combs above the respective $P(E_T)$ spectra indicate the maximum E_T value for the specified co-fragment formed with the probed $CH_3(v=0)$ species.

View Article Online
DOI: 10.1039/D5SC04716A

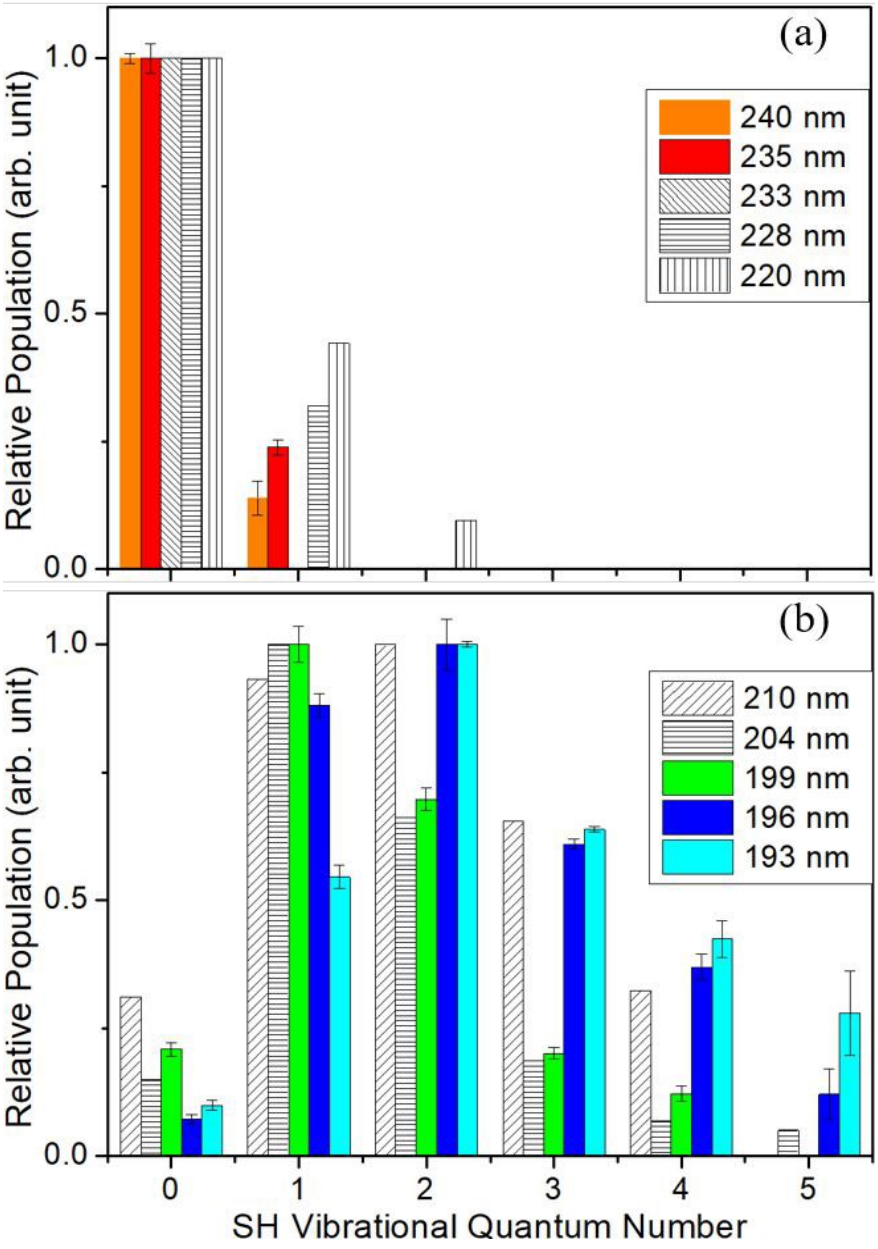

Figure 3. SH $P(v)$ distributions from photolysis of a jet-cooled CH_3SH sample deduced from analysing $CH_3(v=0)$ images measured at λ = (a) 240 and 235 nm (present work) and 233, 228 and 220 nm (from ref. 35) and (b) 210 nm (ref. 42), 204 nm (ref. 41), 199, 196 and 193 nm (present work), in each case normalized such that the most populated level is plotted with unit intensity. The error bars represent the standard error in the simulation, but do not allow for the likely overestimation of the relative population in the highest v levels (see Section 3.1).

View Article Online
DOI: 10.1039/D5SC04716A

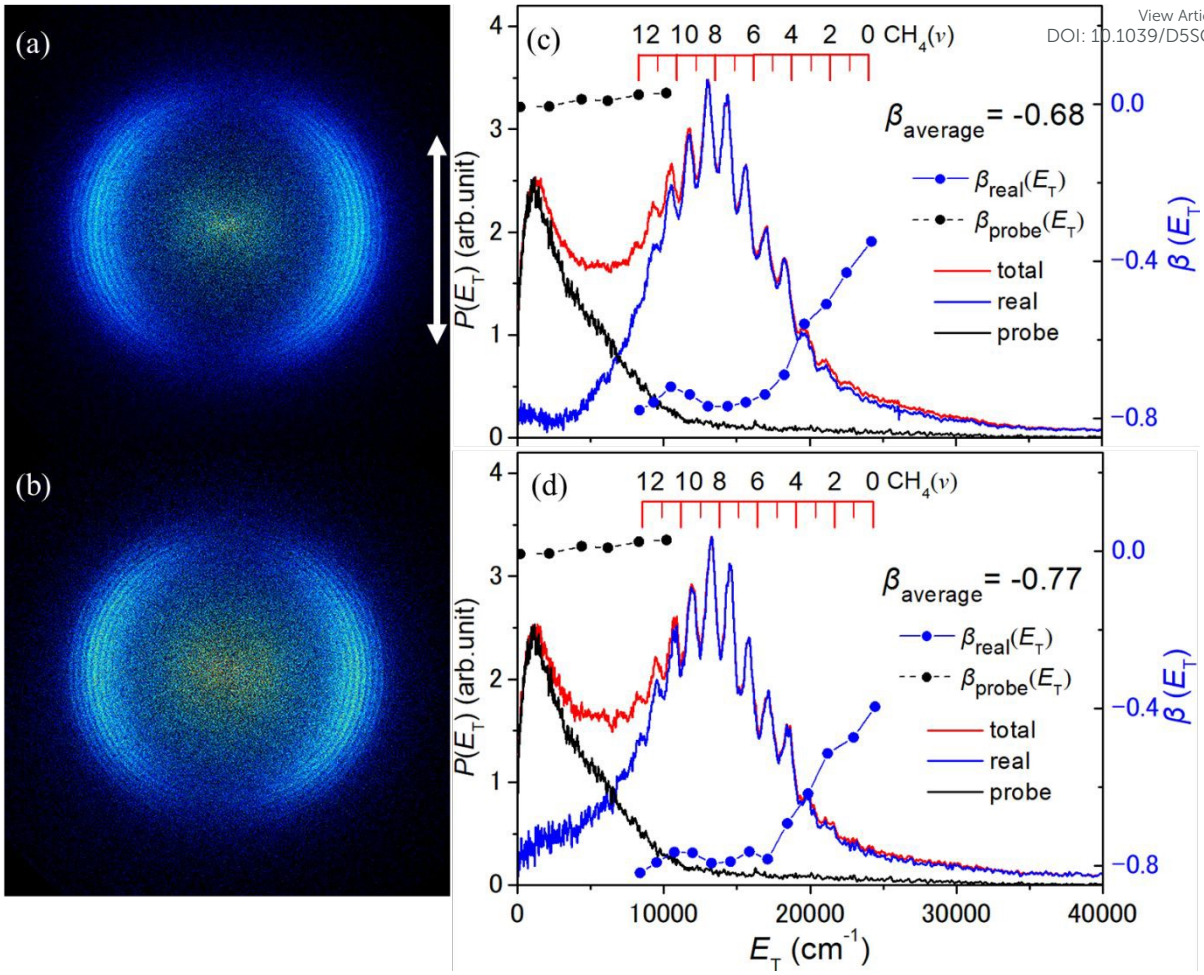

Figure 4. TS-VM images of the S(^{1}D) fragments formed by photolysis of jet-cooled CH_3SH molecules at λ = (a) 192 and (b) 191 nm, with $\boldsymbol{\varepsilon}_{\mathbf{phot}}$ aligned vertically in the plane of the image as indicated by the double headed arrow in (a). Panels (c) and (d) show the $P(E_T)$ distributions derived from this two-colour image (red trace), from the 130.091 nm probe-laser only image (black trace) and the 'real' pump-probe two-colour $P(E_T)$ distribution obtained from the difference (blue trace), referenced to the left-hand *y*-axis scale. The black and blue dots show the $\beta(E_T)$ distributions derived from the corresponding traces, referenced to the right-hand *y*-axis scale. The $\beta_{average}$ value for the signal from photolysis laser induced dissociation determined over the indicated E_T range is also included in the inset. The red combs in panels (c) and (d) show the maximum E_T values for different S(^{1}D) + $CH_4(v_4)$ product channels.

View Article Online
DOI: 10.1039/D5SC04716A

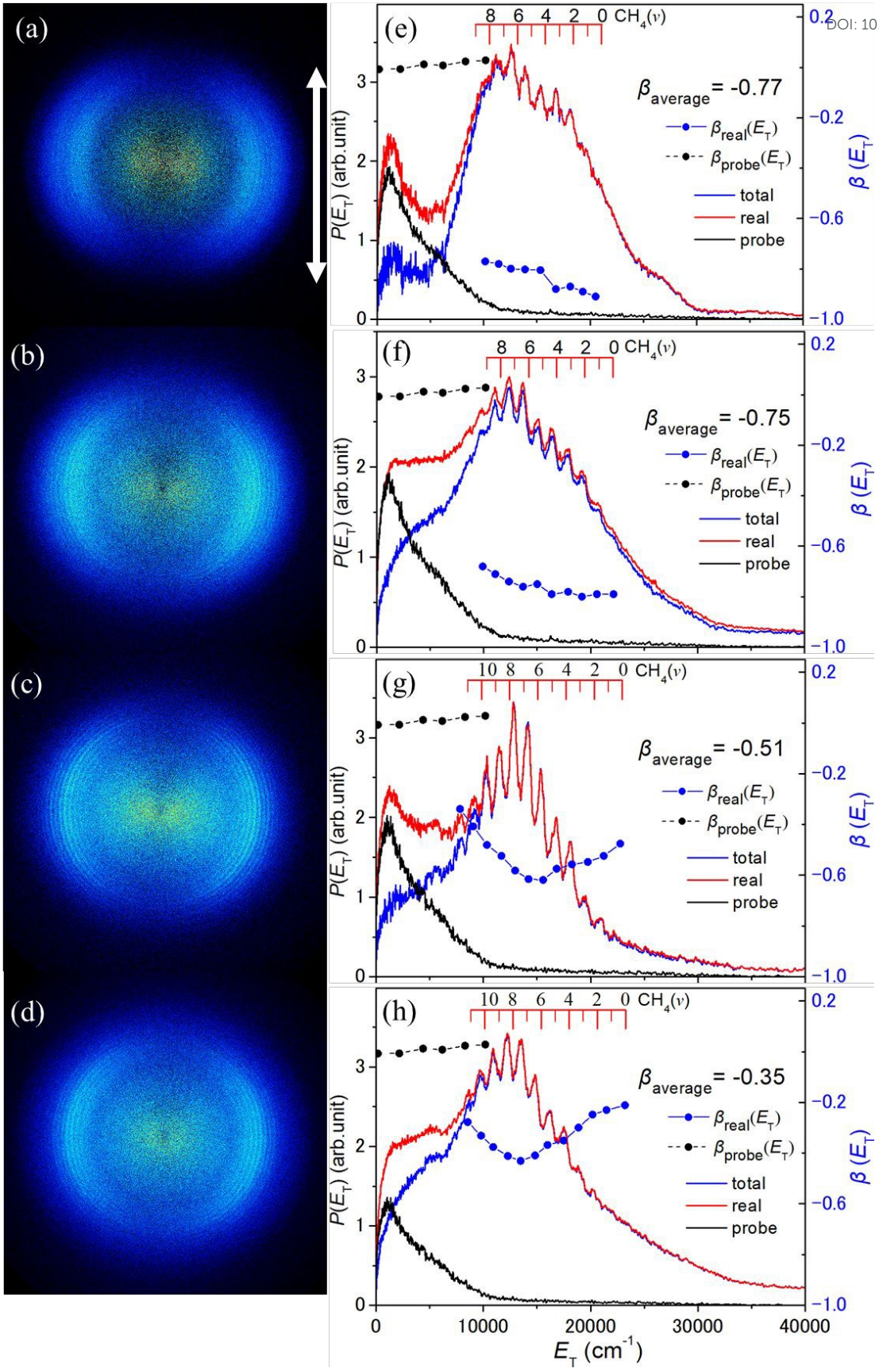

View Article Online
DOI: 10.1039/D5SC04716A

Figure 5. TS-VM images of the S(^{1}D) fragments formed by photolysis of jet-cooled CH_3SH molecules at λ = (a) 204, (b) 199, (c) 196 and (d) 193 nm, with $\boldsymbol{\varepsilon_{phot}}$ aligned vertically in the plane of the image as indicated by the double headed arrow in (a). Panels (e) – (h) show the $P(E_T)$ distributions derived from each two-colour image (red trace), from the 130.091 nm probe-laser only image (black trace) and the 'real' pump-probe two-colour $P(E_T)$ distribution obtained from the difference (blue trace), referenced to the left-hand *y*-axis scale. The black and blue dots show the $\beta(E_T)$ distributions derived from the corresponding traces, referenced to the right-hand *y*-axis scale. The $\beta_{average}$ value for the signal from photolysis laser induced dissociation determined over the indicated E_T range.

View Article Online
DOI: 10.1039/D5SC04716A

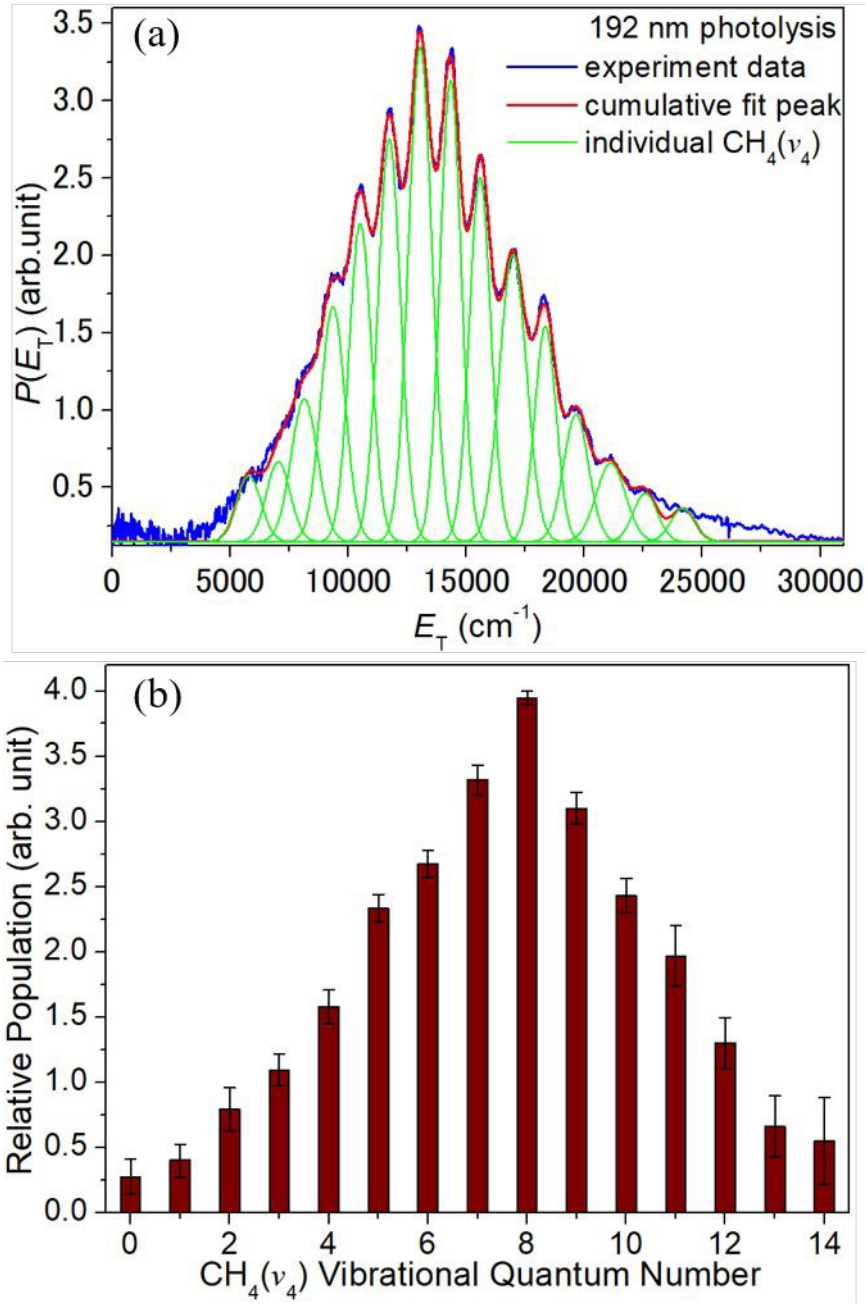

Figure 6. (a) Illustrative decomposition of the $P(E_T)$ spectrum obtained from analysis of the TS-VM image of the S(^{1}D) fragments formed by photolysis of jet-cooled CH_3SH molecules at $\lambda = 192$ nm using Gaussian functions to describe the relative populations in the partner $CH_4(v_4)$ levels. (b) Histogram illustrating the inverted CH_4 $P(v_4)$ vibrational population distribution so derived. The error bars represent the standard error in the simulation.

View Article Online
DOI: 10.1039/D5SC04716A

References

[1] R. Jackson and A. Gabric, *Microorganisms* 2022, **10**, 1581.
[2] R.P. Kiene, *Mar. Chem*. 2020, **54**, 69–83.
[3] C.L. Lee and P. Brimblecombe, *Earth Sci. Rev*. 2016, **160**, 1-18.
[4] S.J. Lawson, C.S. Law, M.J. Harvey, T.G. Bell, C.F. Walker, W.J. de Bruyn and E.S. Saltzman, *Atmos. Chem. Phys.* 2020, **20**, 3061-3078.
[5] G.A. Novak, D.B. Kilgour, C.M. Jernigan, M.P. Vermeuel and T.H. Bertram, *Atmos. Chem. Phys*. 2022, **22**, 6309-6325.
[6] V. Gros, B. Bonsang, R. Sarda-Estève, A. Nikolopoulos, K. Metfies, M. Wietz and I. Peeken, *Biogeosciences* 2023, **20**, 851-867.
[7] C. Wohl, G.L. Forster, P.M. Edwards, P. Suntharalingam and D.E. Oram, *Geophys. Res. Letts.* 2025, **52**, e2025GL114929.
[8] M. Rocco, E. Dunne, R. Salignat, A. Saint-Macary, M. Peltola, T. Barthelmeβ, G. Chamba, N. Barr, K. Safi, A. Marriner, S. Deppeler, C. Rose, J. Uitz, J. Harnwell, A. Engel, A. Colomb, A. Saiz-Lopez, M.J. Harvey, C.S. Law and K. Sellegri, *J. Geophys. Res. Atmospheres* 2025, **130**, e2024JD041072.
[9] G.S. Tyndall and A.R. Ravishankara, *Int. J. Chem. Kin.* 1991, **23**, 483-527.
[10] M. Asplund, N. Grevesse, A.J. Sauval and P. Scott, *Ann. Rev. Astron. Astrophys*. 2009, **47**, 481-522.
[11] D.E. Anderson, E.A. Bergin, S. Maret and V. Wakelam, *Astrophys. J.* 2013, **779**, 141.
[12] T.H.G. Vidal, J.-C. Loison, A.Y. Jaziri, M. Ruaud, P. Gratier and V. Wakelam, *Mon. Not. R. Astron. Soc*. 2017, **469**, 435-447.
[13] S. Narayanan, E.L. Piacentino, K.I. Öberg and M. Rajappan, *Astrophys. J.* 2025, **986**, 10.
[14] B.E. Turner, *Astrophys. J.* 1977, **213**, L75.
[15] R.A. Linke, M.A. Frerking and P. Thaddeus, *Astrophys. J.* 1979, **234**, L139.
[16] E. Gibb, A. Nummelin, W.M. Irvine, D.C.B. Whittet and P. Bergman, *Astrophys. J.* 2000, **545**, 309.
[17] G. Cernicharo, N. Marcelino, E. Roueff, M. Gerin, A. Jiménez-Escobar and G.M. Muñoz, *Astrophys. J.* 2012, **759**, L43.
[18] L. Kolesniková, B. Tercero, J. Cernicharo, J.L. Alonso, A.M. Daly, B.P. Gordon and S.T. Shipman, *Astrophys. J.* 2014, **784**, L7.
[19] L. Majumdar, P. Gratier, T. Vidal, V. Wakelam, J.-C. Loison, K.M. Hickson and E. Caux, *Mon. Not. R. Astron. Soc*. 2016, **458**, 1859.
[20] C. Vastel, D. Quénard, R. Le Gal, V. Wakelam, A. Andrianasolo, P. Caselli, T. Vidal, C. Ceccarelli, B. Lefloch and R. Bachiller, *Mon. Not. R. Astron. Soc*. 2018, **478**, 5514.
[21] M. el Akel, L.A. Kristensen, R. Le Gal, S.J. van der Walt, R.L. Pitts and F. Dulieu, *Astron. Astrophys*. 2022, **659**, A100.
[22] L. Bouscasse, T. Csengeri, A. Belloche, F. Wyrowski, S. Bontemps, R. Güsten and K.M. Menten, *Astron. Astrophys*. 2022, **662**, A32.
[23] N. Madhusudhan, S. Constatinou, M. Holmberg, S. Sarkar, A.A.A. Piette and J.I. Moses, *Astrophys. J. Lett*. 2025, **983**, L40.

View Article Online
DOI: 10.1039/D5SC04716A

[24] N. Hänni, K. Altwegg, M. Combi, S.A. Fuselier, J. De Keyser, N.F.W. Ligterink, M. Rubin and S.F. Wampfler, *Astrophys. J.* 2024, **976**, 74.
[25] N.W. Reed, R.L. Shearer, S.E. McGlynn, B.A. Wing, M.A. Tolbert and E.C. Browne, *Astrophys. J. Lett.* 2024, **973**, L38.
[26] W.C. Price, J.P. Teegan and A.D. Walsh, *Proc. Roy. Soc. (London) A* 1950, **201**, 600-609.
[27] L.B. Clark and W.T. Simpson, *J. Chem. Phys*. 1965, **43**, 3666-3672.
[28] I. Tokue, A. Hiraya and K. Shobotake, *Chem. Phys*. 1987, **116**, 449-456.
[29] G.L. Vaghjiani, *J. Chem. Phys*. 1993, **99**, 5936-5943.
[30] S. Choi, T.Y. Kang, K.-W. Choi, S. Han, D.-S. Ahn, S.J. Baek and S.K. Kim, *J. Phys. Chem. A* 2008, **112**, 7191-7199.
[31] J.E. Stevens, K.F. Freed, M.F. Arendt and R.L. Graham, *J. Chem. Phys*. 1994, **101**, 4832-4841.
[32] J.E. Stevens, H.W. Jang, L.J. Butler and J.C. Light, *J. Chem. Phys*. 1995, **102**, 7059-7069.
[33] S.H.S. Wilson, M.N.R. Ashfold and R.N. Dixon, *J. Chem. Phys*. 1994, **101**, 7538-7547.
[34] J. Segall, Y. Wen, R. Singer, M. Dulligan and C. Wittig, *J. Chem. Phys*. 1993, **99**, 6600-6606.
[35] G.A. Amaral, F. Ausfelder, J.G. Izquierdo, L. Rubio-Lago and L. Bañares, *J. Chem. Phys*. 2007, **126**, 024301.
[36] E. Jensen, J.S. Keller, G.C.G. Waschewsky, J.E. Stevens, R.L. Graham, K.F. Freed and L.J. Butler, *J. Chem. Phys*. 1993, **98**, 2882-2890.
[37] S.B. Barone, A.A. Turnipseed, T. Gierczak and A.R. Ravishankara, *J. Phys. Chem*. 1994, **98**, 11969-11977.
[38] D.R. Yarkony, *J. Chem. Phys*. 1996, **104**, 3639-3644.
[39] D.R. Yarkony, *J. Chem. Phys*. 1996, **104**, 7866-7881.
[40] J.G. Izquierdo, G.A. Amaral, F. Ausfelder, F.J. Aoiz and L. Bañares, *ChemPhysChem* 2006, **7**, 1682-1686.
[41] Z.C. Chen, Q. Shuai, A.T.J.B. Eppink, B. Jiang, D.X. Dai, X.M. Yang and D.H. Parker, *Phys. Chem. Chem. Phys*. 2011, **13**, 8531-8536.
[42] D.V. Chicharro, S.M. Poullain, L. Rubio-Lago and L. Bañares, *J. Phys. Chem. A* 2019, **123**, 8552-8561.
[43] B. Ruscic and D.H. Bross, Active Thermochemical Tables (ATcT) values based on ver. 1.202 of the Thermochemical Network (2024); available at ATcT.anl.gov.
[44] A. Kramida, Yu. Ralchenko, J. Reader and NIST ASD Team (2024). *NIST Atomic Spectra Database* (ver. 5.12), [Online]. Available: https://physics.nist.gov/asd [2025, June 05]. National Institute of Standards and Technology, Gaithersburg, MD. DOI: https://doi.org/10.18434/T4W30F.
[45] M.E. Jacox, *J. Phys. Chem. Ref. Data* 1988, **17**, 269-511, and references therein.
[46] D. Kamra and J.M. White, *J. Photochem*. 1975, **4**, 361-373.
[47] S. Nourbakhsh, K. Norwood, H.-M. Yin, C.-L. Liao and C.Y. Ng, *J. Chem. Phys*. 1991, **95**, 946-954.
[48] C.-W. Hsu, C.-L. Liao and C.-Y. Ng, *J. Chin. Chem. Soc*. 1995, **42**, 149-155.

View Article Online
DOI: 10.1039/D5SC04716A

[49] Y. Chang, S.R. Yu, Q.M. Li, Y. Yu, H.L. Wang, S. Su, Z.C. Chen, L. Che, X.G. Wang, W.Q. Zhang, D.X. Dai, G.R. Wu, K.J. Yuan and X.M. Yang, *Rev. Sci. Instrum.* 2018, **89**, 063113.

[50] J.M. Zhou, Y.R. Zhao, C.S. Hansen, J.Y. Yang, Y. Chang, Y. Yu, G.K. Cheng, Z.C. Chen, Z.G. He, S.R. Yu, H.B. Ding, W.Q. Zhang, G.R. Wu, D.X. Dai, C.M. Western, M.N.R. Ashfold, K.J. Yuan and X.M. Yang, *Nat. Commun*. 2020, **11**, 1547.

[51] Z.X. Li, M. Zhao, T. Xie, Z.J. Luo, Y. Chang, G.K. Cheng, J.Y. Yang, Z.C. Chen, W.Q. Zhang, G.R. Wu, X.G.Wang, K.J. Yuan and X.M. Yang, *J. Phys. Chem. Lett.* 2021, **12**, 844-849.

[52] Z.X. Li, Y.L. Fu, Z.J. Luo, S.K. Yang, Y.C. Wu, H. Wu, G.R. Wu, W.Q. Zhang, B.N. Fu, K.J. Yuan, D.H. Zhang and X.M. Yang, *Science* 2024, **383**, 746-750.

[53] S.K. Yang, Y.C. Wu, Z.J. Luo, Z.X. Li, W. Hua, Y. Chang, X.G. Wang, K.J. Yuan and X.M. Yang, C. *Chin. J. Chem. Phys*. 2024, **37**, 286-294.

[54] Y. Chang, M.N.R. Ashfold, K.J. Yuan and X.M. Yang, *Natl. Sci. Rev.* 2023, **10**, nwad158.

[55] Y.R. Zhao, Z.J. Luo, Y. Chang, Y.C. Wu, S.E. Zhang, Z.X. Li, H.B. Ding, G.R. Wu, J.S. Campbell, C.S. Hansen, S.W. Crane, C.M. Western, M.N.R. Ashfold, K.J. Yuan and X.M. Yang, *Nat. Comm*. 2021, **12**, 4459.

[56] Y.R. Zhao, J.J. Chen, Z.J. Luo, Y. Chang, J.Y. Yang, W.Q. Zhang, G.R. Wu, S.W. Crane, C.S. Hansen, H.B. Ding, F. An, X.X. Hu, D.Q. Xie, M.N.R. Ashfold, K.J. Yuan and X.M. Yang, *Chem. Sci*. 2023, **14**, 2501-2517.

[57] Z.C. Chen, A.T.J.B. Eppink, B. Jiang, G.C. Groenenboom, X.M. Yang and D.H. Parker, *Phys. Chem. Chem. Phys*. 2011, **13**, 2350-2355.

[58] S. Mondal and K.P. Liu, *J. Phys. Chem. A* 2019, **123**, 1514-1520.

[59] Y.C. Wu, Z.J. Luo, S.K. Yang, S.J. McGoldrick, J.L. Mendham, Z.X. Li, S.Y. Zhou, Y.X. Dong, D.X. Dai, C.S. Hansen, M.N.R. Ashfold, K.J. Yuan and X.M. Yang, *J. Chem. Phys*. (submitted).

[60] A.B. Callear and D.R. Dickson, *Trans. Faraday Soc*. 1970, **66** 1987-1995.

[61] C. Anastasi, M. Broomfield, O.J. Nielsen and P. Pagsberg, *Chem. Phys. Lett.* 1991, **182**, 643-648.

[62] A. Kumar, P.K. Chowdhury, K.V.S.R. Rao and J.P. Mittal, *Chem. Phys. Lett*. 1992, **198**, 406-412.

[63] R.T. Bise, H. Choi, H.B. Pedersen, D.H. Mordaunt and D.M. Neumark, *J. Chem. Phys*. 1999, **110**, 805-816.

[64] C.-P. Liu, Y. Matsuda and Y.-P. Lee, *J. Chem. Phys*. 2003, **119**, 12335-12341.

[65] V. Boudon, M. Rey and M. Loëte, *J. Quant. Spectrosc. Rad. Trans*. 2006, **98**, 394-404.

[66] K. Kefala, V. Boudon, S.N. Yurchenko and J. Tennyson, *J. Quant. Spectrosc. Rad. Trans*. 2024, **316**, 108897.

[67] Y. Chang, F. An, Z.C. Chen, Z.J. Luo, Y. Zhao, X.X. Hu, J.Y. Yang, W.Q. Zhang. G.R. Wu, D.Q. Xie, K.J. Yuan and X.M. Yang, *Nat. Commun*. 2021, **12**, 6303.

[68] Y.R. Shao, J.J. Chen, Z.J. Luo, Z.X. Li, S.K. Yang, Y. Chang, F. An, Z.C. Chen, J.Y. Yang, G.R. Wu, W.Q. Zhang, X.X. Hu, D.Q. Xie, H.B. Ding, K.J. Yuan and X.M. Yang, *J. Phys. Chem. Letts*. 2022, **13**, 9786-9792.

[69] L. Zhou, Y.C. Chang, Q.-Z. Yin and W.M. Jackson, *Science* 2014, **346**, 61-64.

View Article Online
DOI: 10.1039/D5SC04716A

[70] W.T. Chen, L. Zhang, D.F. Yuan, Y. Chang, S.R. Yu, S.W. Wang, T. Wang, B. Jiang, K.J. Yuan, X.M. Yang and X.G. Wang, *J. Phys. Chem. Letts*. 2019, **10**, 4783-4787.

[71] Y. Chang, Y.L. Fu, Z.C. Chen, Z.J. Luo, Y.R. Zhao, Z.X. Li, W.Q. Zhang, G.R. Wu, B.N. Fu, D.H. Zhang, M.N.R. Ashfold, X.M. Yang and K.J. Yuan, *Chem. Sci*. 2023, **14**, 8255-8261.

[72] J.O. Thomas, K.E. Lower and C. Murray, *J. Phys. Chem. Lett*. 2012, **3**, 1341-1345.

[73] J.O. Thomas, K.E. Lower and C. Murray, *J. Phys. Chem. A*. 2014, **118**, 9844-9852.

[74] A.G. Suits, *Acc. Chem. Res*. 2008, **41**, 873-881.

[75] E. Herbst and E.F. van Dishoeck, *Annu. Rev. Astron. Astrophys*. 2009, **47**, 427-480.

[76] V. Bariosco, L. Tinacci, S. Pantaleone, C. Ceccarelli, A. Rimola and P. Ugliengo, *Mon. Not. R. Astron. Soc.* 2025, **539**, 82-94 and references therein.

View Article Online
DOI: 10.1039/D5SC04716A

The data supporting this study are available within the main text and the ESI.